



# Tin antimony sulfide ( $\text{Sn}_6\text{Sb}_{10}\text{S}_{21}$ ) thin films by heating chemically deposited $\text{Sb}_2\text{S}_3/\text{SnS}$ layers: Studies on the structure and their optoelectronic properties

Sebin Devasia <sup>a</sup>, S. Shaji <sup>a, b</sup>, D.A. Avellaneda <sup>a</sup>, J.A. Aguilar Martinez <sup>a, c</sup>, B. Krishnan <sup>a, b, \*</sup>

<sup>a</sup> Facultad de Ingeniería Mecánica y Eléctrica, Universidad Autónoma de Nuevo León, San Nicolás de los Garza, Nuevo León, 66455, Mexico

<sup>b</sup> Centro de Innovación, Investigación y Desarrollo en Ingeniería y Tecnología (CIIDIT)- Universidad Autónoma de Nuevo León, Parque de Investigación e Innovación Tecnológica (PIIT), Apodaca, Nuevo León, 66600, Mexico

<sup>c</sup> Centro de Investigación e Innovación en Ingeniería Aeronáutica (CIIIA), Facultad de Ingeniería Mecánica y Eléctrica, Carretera a Salinas Victoria, Apodaca, Nuevo León, 66600, Mexico



## ARTICLE INFO

### Article history:

Received 3 December 2019

Received in revised form

7 February 2020

Accepted 9 February 2020

Available online 11 February 2020

### Keywords:

Tin antimony sulfide

Thin film

Chemical bath deposition

Photoconductivity

Solar cell

## ABSTRACT

Tin antimony sulfide thin films ( $\text{Sn}_6\text{Sb}_{10}\text{S}_{21}$ ) were obtained on glass substrates by heating chemical bath deposited  $\text{Sb}_2\text{S}_3/\text{SnS}$  layers. The report primarily focuses on the structure, composition, morphology, optical and electrical properties of the thin films formed at the temperature range of 300–450 °C for 30 min as well as at the optimized temperature of 390 °C for 1, 2 and 3 h in low vacuum. X-ray diffraction and Raman analysis revealed the crystallization of ternary phase  $\text{Sn}_6\text{Sb}_{10}\text{S}_{21}$  at temperatures higher than 390 °C. X-ray photoelectron study identified the presence of  $\text{Sn}^{2+}$ ,  $\text{Sb}^{3+}$  and  $\text{S}^{2-}$  states in the ternary phase and the depth profile analysis exhibited a uniform distribution of elements throughout the thickness. Further, surface morphology of the as-deposited and annealed thin films were examined using scanning electron microscopy. The optical band gaps calculated from the UV–Vis–NIR spectra were in the range of 1.26–1.45 eV with significantly high absorption coefficients ( $\sim 10^5 \text{ cm}^{-1}$ ) which is ideal for photovoltaic conversion. Moreover, the thin films were photoconductive and when incorporated into the photovoltaic structure, Glass/FTO/Cds/ASTS/C–Ag, demonstrated photovoltaic performance. The corresponding parameters  $V_{oc}$ ,  $J_{sc}$ , and FF were evaluated from the J-V curves yielding the values 409 mV,  $1.46 \text{ mAcm}^{-2}$  and 0.25 respectively.

© 2020 Elsevier B.V. All rights reserved.

## 1. Introduction

A great interest to explore novel materials for thin film photovoltaic technology have led to the realization of advanced materials such as copper indium gallium selenide (CIGS) [1], copper indium disulfide ( $\text{CuInS}_2$ ) [2–4], cadmium telluride ( $\text{CdTe}$ ) [5], Rhenium disulfide  $\text{ReSe}_2$  [6] etc. in the past few decades. However, recent surge in the demand for non-toxic and earth abundant materials to hurdle the toxicity and high processing cost issues have driven the research groups in search for potential substitutes [7]. In this regard, chalcogenides composed of Cu, Sb, Zn and Sn are gaining worldwide attention. Among these, ternary compound tin antimony sulfide ( $\text{Sn–Sb–S}$ ) has been suggested to explore as a

photovoltaic absorber [8–14].

$\text{Sn–Sb–S}$  systems belong to the family of sulfosalts that have a complex chemistry of  $\text{A}_x\text{ByX}_z$ , where A corresponds to metallic atoms like  $\text{Cu}^{1+}$ ,  $\text{Ag}^{1+}$ ,  $\text{Pb}^{2+}$ ,  $\text{Sn}^{2+}$ ,  $\text{Sn}^{4+}$ ,  $\text{Fe}^{2+}$ ,  $\text{Mn}^{2+}$ , etc. B is semi-metallic atoms such as  $\text{Sb}^{3+}$ ,  $\text{As}^{3+}$  and  $\text{Bi}^{3+}$  and X is  $\text{S}^{2-}$ ,  $\text{Se}^{2-}$  and  $\text{Te}^{2-}$  [10,14–16]. The possible applications of the sulfosalts include phase change memory devices [17], catalysis [18], X-ray detectors [19], thermoelectric energy conversion [20], cryoelectronics [21] and thin film photovoltaics [10]. The molecular model for  $\text{Sn–Sb–S}$  system proposes that while the Sb atom bonds covalently with surrounding three S atoms, each Sn atom bonds with four S atoms leading to the pyramidal [ $\text{Sb}_3\text{S}_3$ ] and tetrahedral [ $\text{SnS}_4$ ] structures linked through S atoms [22].

Dittrich et al. reported the first solar cell based on  $\text{Sn–Sb–S}$  ternary absorber material that showed a PCE of 1.05%. These solar cells similar to CIGS technology were fabricated with the structure of  $\text{Mo/Sn–Sb–S absorber/ZnO(Al)}$  by thermal evaporation [14,23].

\* Corresponding author. Facultad de Ingeniería Mecánica y Eléctrica, Universidad Autónoma de Nuevo León, San Nicolás de los Garza, Nuevo León, 66455, Mexico.

E-mail address: [kbindu\\_k@yahoo.com](mailto:kbindu_k@yahoo.com) (B. Krishnan).

Since then, various Sn–Sb–S systems have been the major center of attention for photovoltaic research. The major Sn–Sb–S phases reported include  $\text{SnSb}_4\text{S}_7$  [22],  $\text{SnSb}_2\text{S}_4$  [22],  $\text{Sn}_2\text{Sb}_2\text{S}_5$  [22,24],  $\text{Sn}_3\text{Sb}_2\text{S}_6$  [9],  $\text{Sn}_2\text{Sb}_6\text{S}_{11}$  [24] and  $\text{Sn}_4\text{Sb}_6\text{S}_{13}$  [9,25]. Interestingly, most of these sulfosalts exhibit band gaps close to 1.3 eV, an optimum value required for an absorber layer to have high power conversion efficiency in solar cells.

Predominantly, vacuum thermal evaporation [13,22,25–27] and sputtering [28] techniques have been used to prepare various phases of Sn–Sb–S thin films till now. Usually in vacuum assisted deposition, the starting material is prepared either by treating Sn, Sb and S at a high temperature range of 600–700 °C for longer durations or by depositing Sn/Sb metal thin films followed by sulfurization [28,29]. Thermally evaporated polycrystalline tin antimony sulfide thin film with  $\text{SnSb}_2\text{S}_4$  and  $\text{Sn}_2\text{Sb}_2\text{S}_5$  phases displayed good photoconductivities with a band gap of 1.6 eV, indicating Sn rich conditions for better photoresponses [27]. Khan et al. fabricated n-type conducting  $\text{Sn}_2\text{Sb}_2\text{S}_5$  polycrystalline thin films via vacuum thermal evaporator using a double source technique and reported absorption coefficients in the order of  $10^5 \text{ cm}^{-1}$  with a direct optical band gap in the range of 1.6–1.7 eV [13]. The reported band gap values, high absorption coefficients and photoconductivity studies indicate that the Sn–Sb–S systems are highly promising for thin film photovoltaics [14].

The scientifically attractive SnS,  $\text{Sb}_2\text{S}_3$  and CZTS sulfosalts have been under research for the last few decades. Despite having a predicted theoretical efficiency of 32% [30], SnS fails to perform well in the photovoltaic structures, only reaching a recent 4.4% of PCE [30,31]. Besides, the nontoxic and stable  $\text{Sb}_2\text{S}_3$  with a direct bandgap of 1.78–2.5 eV and high absorption coefficients ( $>10^5 \text{ cm}^{-1}$ ) has been also studied in detail for photovoltaic applications. However, the chalcogenide usually demonstrates highly resistive character limiting their efficiencies [32]. The solar cells based on  $\text{Sb}_2\text{S}_3$  layer showed only an efficiency as high as 5.4%, reported by Deng et al. [33]. Another interesting material investigated in this group is the quaternary  $\text{Cu}_2\text{ZnSnS}_4$  (CZTS) which have yielded a PCE up to 12.6% when incorporated into a solar cell structure [34]. Even though various efforts were made to suppress the  $\text{Cu}_{\text{Zn}}$  antisite defects, the significant voltage loss as compared to the absorber bandgap and  $qV_{\text{oc}}$  is hindering their application in devices [35–37]. Compared to SnS or  $\text{Sb}_2\text{S}_3$ , the ternary compounds of tin antimony sulfide demonstrate stable p-type behavior with direct band gaps in the range of 1.2–1.7 eV, highly favorable for reaching maximum efficiencies as per Shockley–Quissner limit [38,39]. In addition, they are comparatively less toxic, abundant, cheap and have good absorption values in the visible spectrum. Therefore, it is important to explore Sn–Sb–S thin film systems through facile methods such as chemical bath deposition. Favorably, the chemical bath deposition(CBD) technique has been used for the deposition of high quality SnS and  $\text{Sb}_2\text{S}_3$  thin films by our group [40–43]. In addition, synthesis of different ternary phases such as  $\text{AgSb}(\text{Se}/\text{S})_2$  and  $\text{CuSb}(\text{S}/\text{Se})_2$  as well as their performance in solar cells have also been extensively studied before [44,45].

Current work discusses the formation  $\text{Sn}_6\text{Sb}_{10}\text{S}_{21}$ , a ternary phase in Sn–Sb–S system through post thermal treatments of  $\text{Sb}_2\text{S}_3/\text{SnS}$  precursor films deposited via CBD, a relatively cost-effective and simple method compared to high vacuum techniques and other complicated processing techniques. To the best of authors knowledge, this is the first report of  $\text{Sn}_6\text{Sb}_{10}\text{S}_{21}$  thin films as well as CBD route to synthesize an Sn–Sb–S ternary phase. Our findings from the present work can greatly contribute to the continued research for photovoltaic devices based on tin antimony sulfide thin films.

## 2. Experimental

### 2.1. Deposition of $\text{Sb}_2\text{S}_3$ thin films

Antimony sulfide thin films were deposited on glass substrates by chemical bath deposition [32]. First, the glass substrates were cleaned thoroughly using sonicator by keeping them in the soap solution, distilled water, isopropanol and distilled water respectively. The chemical bath was prepared by dissolving 0.325 g of antimony trichloride ( $\text{SbCl}_3$ , 99.99%) in 1.2 ml acetone followed by adding 12.5 ml sodium thiosulfate ( $\text{Na}_2\text{S}_2\text{O}_3 \cdot 5\text{H}_2\text{O}$ , 99.99%) and 32.5 ml deionized water. For the deposition, the glass substrates were arranged horizontally in the precursor solution for 2 h at a temperature of 25 °C. Finally, the thin films on glass substrates were washed in running distilled water and then dried in warm air. The uniform film deposited on the bottom side was used for further procedure and the powdery top surface of the glass slides was cleaned with diluted HCl using cotton balls.

### 2.2. Deposition of $\text{Sb}_2\text{S}_3/\text{SnS}$ layered structure

On top of the  $\text{Sb}_2\text{S}_3$  layer(AS), SnS (TS) thin film was chemically deposited by the following procedure. A 0.044 M precursor solution was prepared from tin(II)chloride dihydrate ( $\text{SnCl}_2 \cdot 2\text{H}_2\text{O}$ ) by dissolving it in 5 ml acetone followed by the addition of 12 ml triethanolamine ( $\text{N}(\text{CH}_2\text{CH}_2\text{OH})_3$ ), 8 ml thioacetamide ( $\text{CH}_3\text{CSNH}_2$ ) and 10 ml ammonium hydroxide. Then the solution was made up to 100 ml by adding deionized water. The  $\text{Sb}_2\text{S}_3$  coated glass slides were kept in the beaker containing precursor solution which was then vertically suspended in a water bath maintained at 55 °C for 4 h. After deposition, the thin films were rinsed thoroughly with distilled water and dried [46].

### 2.3. Post deposition thermal treatments

The as-deposited ( $\text{Sb}_2\text{S}_3/\text{SnS}$ ) thin films were heated in low vacuum to produce the ternary Sn–Sb–S phase. The thermal treatments were done at temperatures: 300, 350, 375, 390, 400 and 450 °C in a low vacuum furnace ( $\sim 1 \times 10^{-2}$  torr) (model: VBF-1200X, MTI corporation) for 30 min. Furthermore, at the optimum temperature (390 °C), the effect of annealing time on  $\text{Sn}_6\text{Sb}_{10}\text{S}_{21}$  was studied: 1, 2 and 3 h. Throughout the discussion, we refer to the samples as ASTS for the as-deposited  $\text{Sb}_2\text{S}_3/\text{SnS}$  and ASTS300, ASTS350, ASTS375, ASTS390, ASTS400 and ASTS450 for different heating temperatures as well as ASTS1H, ASTS2H and ASTS3H for various heating durations.

### 2.4. PV device fabrication: FTO/CdS/Sn–Sb–S/C–Ag

The Sn–Sb–S thin film was incorporated as an absorber layer in the photovoltaic structure: Glass/FTO/CdS/ASTS/C–Ag. Initially, the window layer CdS was deposited on the commercial FTO coated glass substrates by chemical bath deposition and then annealed in air at 400 °C for 1 h as in our previous report [47]. Then,  $\text{Sb}_2\text{S}_3$  and SnS thin films were deposited sequentially by CBD as described in sections 2.1 and 2.2. Further, the entire structure was annealed at 390 °C for 15 min in vacuum for the conversion to tin antimony sulfide phase. Finally, the carbon and Ag contacts were applied on the top in an area of  $0.4 \text{ cm}^2$  forming the photovoltaic structure: Glass/FTO/CdS/Sb–Sn–S/C–Ag.

### 2.5. Characterization

The crystallographic studies of the thin films treated at different conditions were carried out from the X-ray diffraction patterns

collected using a PANalytical EMPYREAN diffractometer with Cu K $\alpha$  ( $\lambda = 1.5406 \text{ \AA}$ ) radiation. A Thermo Scientific DXR Raman microscope was employed for measuring the Raman spectra of the samples. The chemical states and elemental composition were analyzed using X-ray photoelectron spectroscopy (Thermo Scientific K-alpha). Further, scanning electron microscopy (SEM-Hitachi SU8020) was used to probe the surface morphology of the thin films. The transmittance, reflectance and absorbance spectra were measured using UV–Vis–NIR (Jasco V770) spectrophotometer. Photocurrent response measurements were done using a Keithley 6487 Picoammeter and a 50 W tungsten halogen lamp. The fabricated photovoltaic devices were characterized (I–V (current–voltage) measurements) in the dark and illumination by a solar simulator (Oriel) of light intensity  $100 \text{ mW/cm}^2$  intensity using an AM1.5 filter.

### 3. Results and discussions

The thickness of the deposited SnS thin film was 220 nm when measured using a stylus profilometer. The approximate thickness required for Sb<sub>2</sub>S<sub>3</sub> thin film to completely react with 220 nm thick SnS to form the Sn<sub>6</sub>Sb<sub>10</sub>S<sub>21</sub> phase can be calculated from their density values (SnS –  $5.22 \text{ gcm}^{-3}$ , Sb<sub>2</sub>S<sub>3</sub> –  $4.64 \text{ gcm}^{-3}$ ) and molecular mass (SnS –  $150.76 \text{ gmol}^{-1}$ , Sb<sub>2</sub>S<sub>3</sub> –  $339.71 \text{ gmol}^{-1}$ ).



The Sb<sub>2</sub>S<sub>3</sub> thickness was around 485 nm and the annealed ASTS thin films had a thickness in the range of 850–950 nm (see Fig. 1).

#### 3.1. X-ray diffraction

The structural evolution of the Sn–Sb–S phase was identified from the X-ray diffraction patterns of the thin films treated at temperatures of 300, 350, 375, 390, 400 and 450 °C in vacuum for 30 min. As it can be seen from Fig. 2, the as-deposited Sb<sub>2</sub>S<sub>3</sub>/SnS thin film show peaks at  $30.51^\circ$  and  $31.53^\circ$  due to the (101) and (111) planes of orthorhombic SnS belonging to Pbnn space group (JCPDS No: 39–0354). When annealed from 300 °C to 390 °C, peaks at

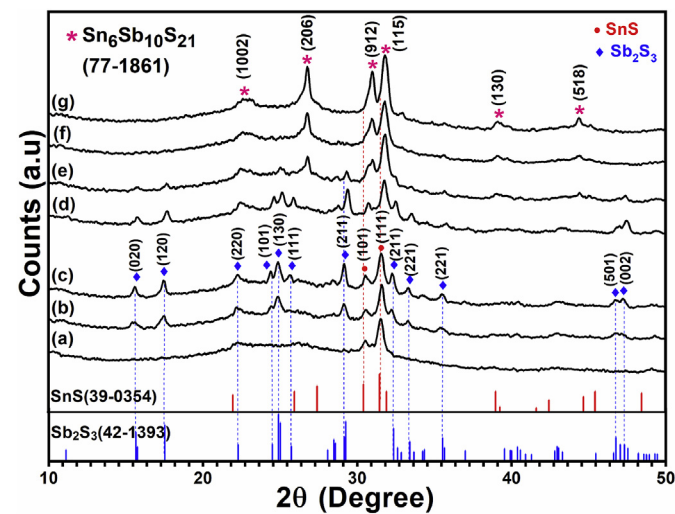


**Fig. 2.** X-ray diffractograms of (a) ASTS, (b) ASTS300, (c) ASTS350, (d) ASTS375, (e) ASTS390, (f) ASTS400 and (g) ASTS450.

$15.6^\circ$ ,  $17.5^\circ$ ,  $22.2^\circ$ ,  $29.1^\circ$ ,  $33.3^\circ$ ,  $35.5^\circ$  and  $47.5^\circ$ , emerged which correspond to the (020), (120), (220), (121), (301), (240) and (511) planes of Sb<sub>2</sub>S<sub>3</sub> crystallized in the orthorhombic structure (JCPDS No: 42–1393). Interestingly, on annealing at temperatures above 390 °C, the peaks corresponding to Sb<sub>2</sub>S<sub>3</sub> disappeared and a shift was observed in the Bragg peak positions towards higher diffraction angles. This indicates that the treatments at high temperatures resulted in the rearrangement of atoms in SnS and Sb<sub>2</sub>S<sub>3</sub> leading to recrystallization of the new ternary phase [48]. The new peaks for ASTS450 were observed at  $26.7^\circ$ ,  $30.9^\circ$ ,  $31.8^\circ$ ,  $39.1^\circ$  and  $44.4^\circ$  which can be assigned respectively to the (206), (912), (115), (130) and (518) planar reflections of the monoclinic Sn<sub>6</sub>Sb<sub>10</sub>S<sub>21</sub> phase (space group C2/m) well in match with the JCPDS file no: 77–1861 as reported by Smith et al. [49]. The absence of any other phases like SnS or Sb<sub>2</sub>S<sub>3</sub> in the samples annealed at 400 and 450 °C suggests the complete conversion of Sb<sub>2</sub>S<sub>3</sub>/SnS layers to the new ternary

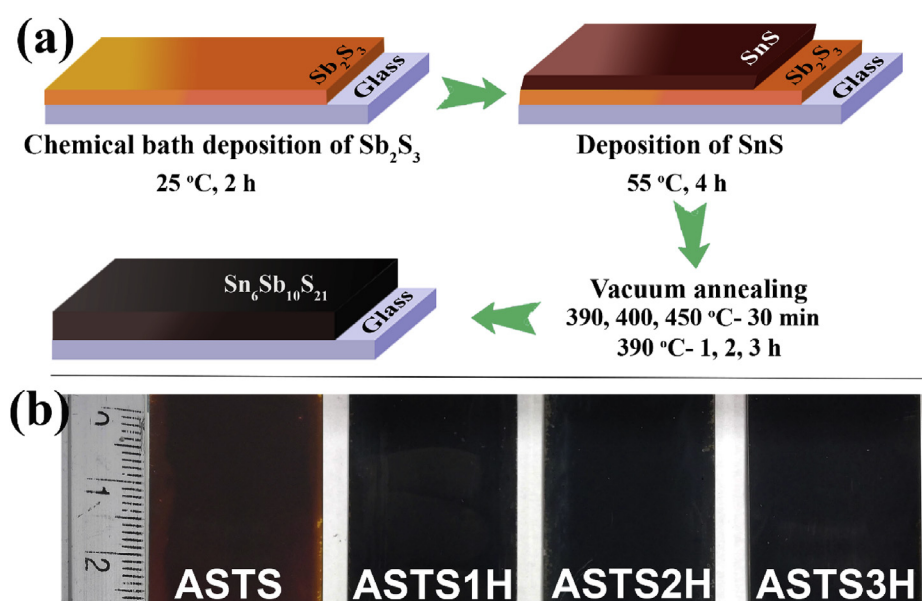


**Fig. 1.** (a) Schematic representation of the sequential deposition of Sb<sub>2</sub>S<sub>3</sub>, SnS and vacuum annealing to obtain Sn<sub>6</sub>Sb<sub>10</sub>S<sub>21</sub> thin films. (b) The as deposited Sb<sub>2</sub>S<sub>3</sub>/SnS (ASTS) thin film and samples annealed at 390 °C for 1 h (ASTS1H), 2 h (ASTS2H) and 3 h (ASTS3H).

phase  $\text{Sn}_6\text{Sb}_{10}\text{S}_{21}$ .

As noted earlier, the amorphous nature of as deposited  $\text{Sb}_2\text{S}_3$  thin films is due to the poor crystalline growth at the lower temperature in chemical bath deposition. Due to the ability to crystallize at lower temperatures, the as prepared  $\text{SnS}$  thin films here have a polycrystalline nature. During the vacuum heat treatments, more tin and antimony atoms diffuse into the other layer and bonds to each other via S atoms [22]. Previous studies on Sn–Sb–S systems show that while  $\text{SnSb}_2\text{S}_4$  crystallizes in the orthorhombic structure,  $\text{Sn}_2\text{Sb}_2\text{S}_5$  and  $\text{Sn}_3\text{Sb}_2\text{S}_6$  crystallize in the monoclinic structure because of the higher Sn concentration. Here, as the concentration of Sn atoms diffusing into the layer increase with thermal treatments, some of the  $\text{Sb}^{3+}$  cations in the orthorhombic structure migrate to the octahedral sites favoring the recrystallization to monoclinic structure [50]. It is relevant to notice the two works of P. Kumar et al. where they use high concentration of  $[\text{SnSe}_4]$  to obtain crystalline  $\text{Sn}_x\text{Sb}_{20}\text{Se}_{80-x}$  samples ( $x > 18$ ) and D. Abdelkader et al. where they use high concentration of  $[\text{SnS}_4]$  to yield different  $\text{Sn}_{2n-4}\text{Sb}_4\text{S}_{2n+2}$  films ( $n = 2.5, 3$  and  $4$ ) [22,51]. These studies comfort the idea that the amount of tin diffusing into other layer is enhancing the bonding in our samples to form the  $\text{Sn}_6\text{Sb}_{10}\text{S}_{21}$  phase during the thermal treatments.

To check further the ternary formation at  $390^\circ\text{C}$ , the samples were annealed at the same temperature for 1 h, 2 h and 3 h in order to study the effect of annealing duration on the crystallinity of new  $\text{Sn}_6\text{Sb}_{10}\text{S}_{21}$  thin films. Fig. 3 illustrates the XRD patterns of ASTS samples annealed at different durations. From the figure, the crystallinity of the sample is enhanced by heat-treating the sample for 2 h at  $390^\circ\text{C}$  whereas further heating for 3 h resulted in reduced crystallinity. The improvement in the crystallinity can be attributed to the better recrystallization of the new phase  $\text{Sn}_6\text{Sb}_{10}\text{S}_{21}$  [48]. A comparison between XRD patterns of individual  $\text{SnS}(\text{TS})$  and  $\text{Sb}_2\text{S}_3(\text{AS})$  layers annealed at  $390^\circ\text{C}$  for 2 h with the ASTS2H is available in supplementary data which shows the ternary phase formation (fig. S-1). From the figure, it is evident that ASTS thin films when annealed at  $390^\circ\text{C}$  for 2 h have very strong peaks at  $26.7^\circ, 30.9^\circ$  and  $31.8^\circ$  different from  $\text{SnS}$  and  $\text{Sb}_2\text{S}_3$  peaks.

The average crystallite size of the thin films was calculated using the Debye-Scherrer equation [52],

$$D = \frac{k\lambda}{\beta \cos \theta} \quad (2)$$

Where,  $D$  is the crystallite size,  $\lambda$  is the wavelength of  $\text{CuK}_{\alpha 1}$

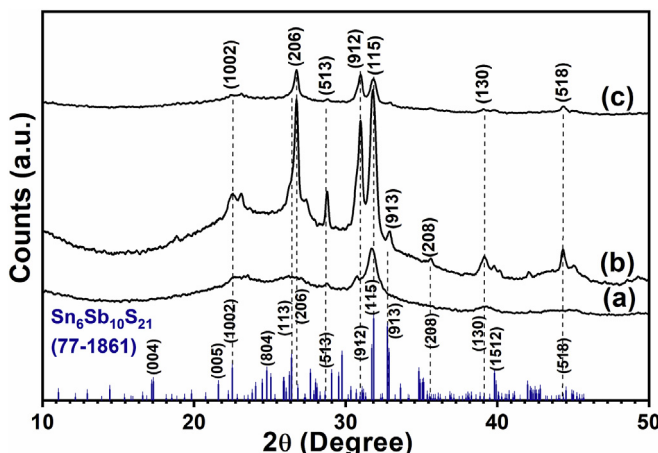


**Fig. 3.** XRD patterns of ASTS thin films annealed at  $390^\circ\text{C}$  for (a) 1 h (ASTS1H), (b) 2 h (ASTS2H) and (c) 3 h (ASTS3H) durations.

radiation ( $=1.5406 \text{ \AA}$ ),  $\beta$  is the full width at half maximum (FWHM),  $\theta$  is the Bragg diffraction angle and  $k$  is the shape factor ( $\sim 0.9$ ). The calculations were done considering the diffraction peak corresponding to (111) peak of  $\text{SnS}$  (annealed below  $390^\circ\text{C}$ ) and (115) and (912) peaks of  $\text{Sn}_6\text{Sb}_{10}\text{S}_{21}$  (annealed at and above  $390^\circ\text{C}$ ). The calculated values of average crystallite size are listed in Table 1.

From the table, the crystallite size values in the range of 15–17 nm for samples heat treated below  $390^\circ\text{C}$ , are that of the  $\text{SnS}$  phase calculated from the (111) peak. The presence of  $\text{Sn}_6\text{Sb}_{10}\text{S}_{21}$  phase was detected in the films formed by heating at  $390^\circ\text{C}$  for 30 min. As the temperature increased, the crystallite size increased due to the further growth of this ternary phase. Hence the smallest crystallite size (15 nm) was for the ASTS390 sample. In the case of ASTS1H (sample annealed at  $390^\circ\text{C}$  for 1 h), the calculated average crystallite size (12 nm) was smaller than that for 30 min sample (ASTS390). The higher crystallite size for ASTS390 can be due to the presence of  $\text{SnS}$  crystallites along with the ternary phase. As the temperature increased, the crystallite size increased due to the improved crystallinity of this ternary phase. However, when annealed at  $390^\circ\text{C}$  for 1 h, smaller crystallites of average size (12 nm) were formed. Such behavior can be associated with the phase transformation and reorientation of atoms of  $\text{SnS}$  and  $\text{Sb}_2\text{S}_3$  during further recrystallization producing smaller  $\text{Sn}_6\text{Sb}_{10}\text{S}_{21}$  grains. Similar results were observed in complex sulfosalts like  $\text{SnBi}_2\text{S}_4$  grown from  $\text{SnS}$  and  $\text{Bi}_2\text{S}_3$  thin films [53]. The increased crystallite size with longer annealing durations suggests the better crystalline growth of the new phase [54].

### 3.2. Raman spectroscopy

To confirm the ternary phase identified from XRD, we measured the Raman spectra of as deposited and annealed ASTS thin films which are illustrated in Fig. 4. The graphs suggest that the Raman peaks are mostly correlated with the vibrations of Sn–S originating from the  $[\text{SnS}_4]$  tetrahedral in the Sn–Sb–S systems. However, a shift in the peaks can be observed as the ASTS thin films are treated at high temperatures. While the major peaks observed for the as-deposited ASTS thin film were at  $92, 147, 175$  and  $220 \text{ cm}^{-1}$ , at higher annealing temperatures they were observed at  $95, 160, 181$  and  $222 \text{ cm}^{-1}$  [9,22,25]. The major shift in peak positions was observed from  $390^\circ\text{C}$  which supports the ternary phase formation as concluded from the X-ray diffraction studies.

When analyzing the Raman shift in the ternary system, it is important to note that the interaction between two or more bonds of similar energies in a molecule can lead to a spectrum slightly different from their individual vibrations [55]. Most importantly,

**Table 1**  
The structural parameters of the ASTS thin films annealed at different temperatures for 30 min and different durations at  $390^\circ\text{C}$ .

Sample	$2\theta (\text{°})$	FWHM ( $\text{°}$ )	Average Crystallite size (nm)
ASTS	31.53	0.4917	16
ASTS300	31.59	0.4763	17
ASTS350	31.56	0.5203	15
ASTS375	31.77	0.5071	16
ASTS390	31.79	0.5513	15
ASTS400	31.77	0.5014	16
ASTS450	31.85	0.4854	17
ASTS1H	31.74 30.81	0.6793 0.6751	12
ASTS2H	31.80 30.93	0.4769 0.5063	16
ASTS3H	31.81 30.94	0.4947 0.4670	17

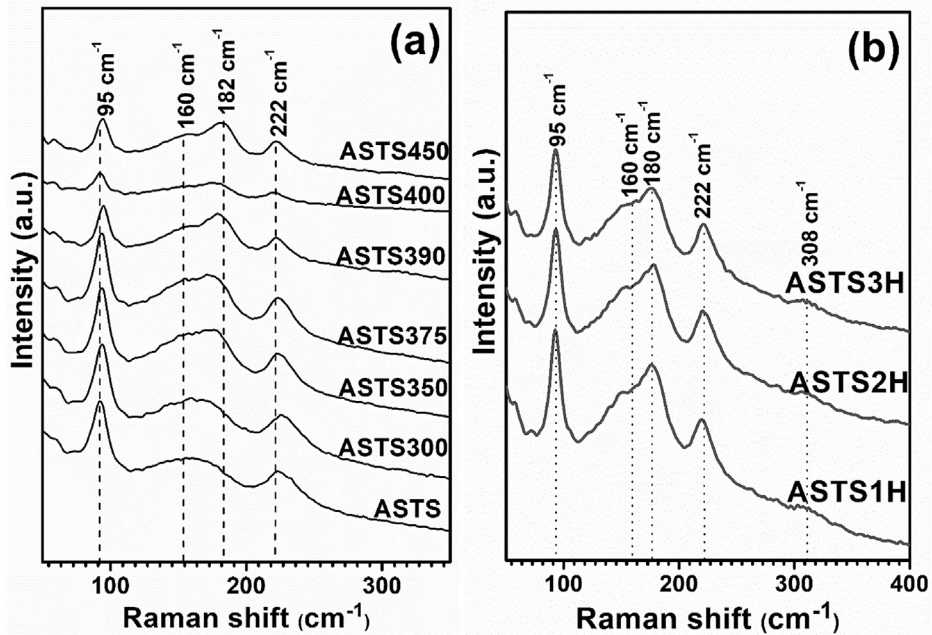


**Fig. 4.** Raman spectra of (a) as prepared ASTS samples as well as the samples annealed at various temperatures in vacuum. (b) ASTS thin films annealed at 390 °C for 1 h, 2 h and 3 h durations.

Sn–Sb–S systems constitute basic structural units of  $\text{SnS}_4$  tetrahedrals and  $\text{SbS}_3$  pyramidal with bridging S atoms. However, the interactions among  $\text{SnS}_4$  and  $\text{SbS}_3$  basic units through the S atom are assumed to be weak [56]. The shift observed in the bands when annealed at higher temperatures may be due to the interactions from  $\text{SbS}_3$  pyramids. Rabeh et al. reported similar results in the case of  $\text{SnSb}_2\text{S}_4$ ,  $\text{Sn}_2\text{Sb}_2\text{S}_5$  and  $\text{Sn}_3\text{Sb}_2\text{S}_6$  thin films. They have also noticed the presence of peaks at 93, 160, 186 and 220  $\text{cm}^{-1}$  in all the Sn–Sb–S systems [50]. In fact, the bands observed at 95  $\text{cm}^{-1}$  and 222  $\text{cm}^{-1}$  can be assigned to the Sn–S vibrational modes in the  $\text{SnS}_4$  tetrahedral units in Sn–Sb–S systems [22,25,50]. The small shoulder at 160  $\text{cm}^{-1}$  was explained to be the net effect of stretching modes in  $\text{SnS}_4$  tetrahedrals and Sb–Sb linkages [22,50]. Further, the peak around 182  $\text{cm}^{-1}$  was ascribed to the Sb–Sb vibrational modes in  $\text{S}_2\text{Sb}$ – $\text{SbS}_2$  units as well as Sn–S vibrations [25,57]. The onset of a very small peak seen in Fig. 4(b) around

308  $\text{cm}^{-1}$  for samples annealed at 390 °C for 2 h and 3 h can be from the asymmetric stretching of Sb–S of  $\text{SbS}_3$  pyramids [50,58,59]. The reported values of Raman modes for different Sn–Sb–S phases and our results are summarized in Table 2.

The results of Raman spectra give more insight into the ternary system which are consistent with the X-ray diffraction studies.

### 3.3. X-ray photoelectron spectroscopy

Chemical states and composition of the elements in the ASTS and ASTS2H samples were determined from XPS spectra as shown in Figs. 5–8. All the spectra were obtained following a soft argon ion etching on the surface and to calibrate the peak binding energy, adventitious carbon at 284.6 eV is used in addition to the charge compensation by the flood gun [32,60]. The peaks obtained were deconvoluted by background calculation employing a Shirley type

**Table 2**  
Raman shifts reported for Sn–Sb–S systems compared with the observed results.

Sn–Sb–S system	Raman shifts ( $\text{cm}^{-1}$ )	Ref.
$\text{SnSb}_4\text{S}_7$	93, 164, 230 and 307 306, 281, 241, 188 and 157 (powder) 295.89, 220.87, 125.51, 165.45, 96.16, 77.88 and 67.69	[22] [9] [25]
$\text{SnSb}_2\text{S}_4$	92, 163, 229 and 307 93, 160, 186 and 220 305, 280, 235 and 194 (powder)	[22] [50] [9]
$\text{Sn}_2\text{Sb}_2\text{S}_5$	313.01, 292.56, 246.88, 158.56, 119.68, 94.89 and 74.69 91, 163, 227 and 307 93, 160, 186 and 220 308, 276, 228 and 176 (powder)	[25] [22] [50] [9]
$\text{Sn}_2\text{Sb}_6\text{S}_{11}$	306, 227.73, 182.19, 148.78, 112.62, 92.02 and 72.49 117, 155, 188, 250, 303, 371 and 450	[25] [57]
$\text{Sn}_3\text{Sb}_2\text{S}_6$	323.76, 309.74, 277.82, 233.45, 135.50, 94.64 and 74.18 93, 160, 186 and 220 306, 271, 227 and 186 (powder)	[50] [9]
$\text{Sn}_4\text{Sb}_6\text{S}_{13}$	296.20, 217.12, 183.31, 152.31, 113.04, 91.84 and 72.35 305, 277, 236 and 197 (powder)	[25] [9]
$\text{Sn}_6\text{Sb}_{10}\text{S}_{21}$	312.44, 246.10, 160.23, 121.99, 97.69, 80.51 and 70.44 95, 160, 180, 222 and 308	[25] [9] Our work

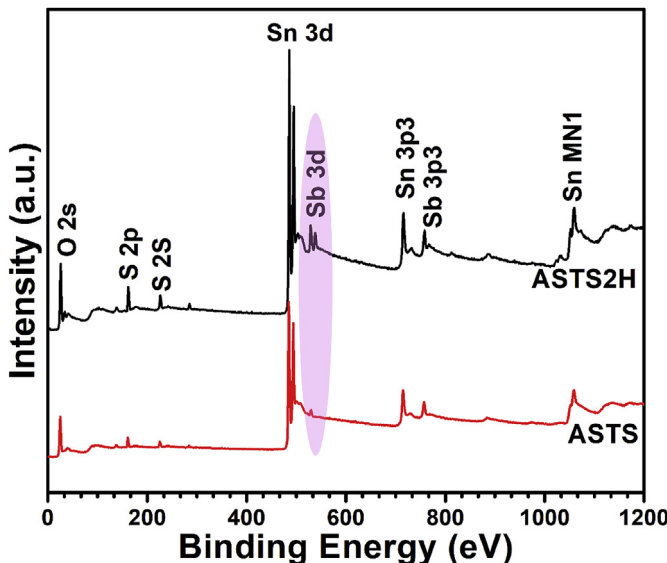


**Fig. 5.** XPS survey spectrum of the ASTS and ASTS2H thin film sample obtained after a soft surface etching.

function followed by peak fitting using the Gaussian-Lorentzian sum function.

From the survey spectra of ASTS and ASTS2H in Fig. 5, we have concluded that the Sb from the bottom layer has successfully diffused to the surface as a result of annealing. Fig. 6(a), (b), (c) and (d) respectively illustrate the high-resolution XPS spectra of Sb3d and S2p levels of Sb<sub>2</sub>S<sub>3</sub> as well as Sn3d and S2p levels of SnS layers

in the as-deposited ASTS sample. The Sb 3d<sub>3/2</sub> and 3d<sub>5/2</sub> peaks were observed at 538.98 eV and 529.58 eV at a spin-orbit doublet separation of 9.4 eV which corresponds to the Sb<sup>3+</sup> in Sb<sub>2</sub>S<sub>3</sub>. As given in Fig. 6(b) the S 2p<sub>1/2</sub> and S 2p<sub>3/2</sub> are located at 162.68 eV and 161.48 eV separated by 1.2 eV consistent with the S<sup>2-</sup> state in Sb<sub>2</sub>S<sub>3</sub> [32]. The peaks observed at 493.18 eV and 484.78 eV in Fig. 6(c) is from the elemental state of Sn whereas the dominant peaks at binding energies of 494.28 eV and 485.88 eV separated by 8.4 eV correspond to Sn 3d<sub>3/2</sub> and Sn 3d<sub>5/2</sub>, respectively, which is assigned to the Sn<sup>2+</sup> state in SnS [60,61]. Further, the peaks corresponding to S2p<sub>1/2</sub> and S2p<sub>3/2</sub> were observed at 161.6 eV and 162.8 eV as shown in Fig. 6(d) which can be attributed to the S<sup>2-</sup> state in SnS [32].

In order to identify the chemical states of Sn, Sb and S in the ternary phase, we studied the XPS spectra of the ASTS thin films annealed at 390 °C for 2 h as seen in Fig. 7(a), (b) and (c). The high resolution spectra for Sn 3d<sub>3/2</sub> and Sn 3d<sub>5/2</sub> show intense peaks at 494.2 eV and 485.78 eV with a spin-orbit separation of 8.42 eV representing Sn<sup>2+</sup> in Sn<sub>6</sub>Sb<sub>10</sub>S<sub>21</sub>. The peaks at 493.08 eV and 484.78 eV are due to the elemental Sn [62]. The peaks of Sb 3d<sub>3/2</sub> and Sb 3d<sub>5/2</sub> at the binding energies of 538.58 eV and 529.19 eV correspond to the 3+ state of Sb with a splitting of 9.39 eV. Besides, the very small peaks at 537.21 eV and 527.82 eV may have arisen from the elemental Sb [62]. Similar values were observed by Zhong et al for Sb 3d<sub>5/2</sub> and Sb 3d<sub>3/2</sub> in Sn<sub>2</sub>Sb<sub>6</sub>S<sub>11</sub> and Sn<sub>2</sub>Sb<sub>2</sub>S<sub>5</sub> phases [24]. As given in Fig. 7(c), the core level S 2p<sub>1/2</sub> and S 2p<sub>3/2</sub> peaks were observed at binding energies 162.39 eV and 161.19 eV at 1.2 eV apart which can be ascribed to the S<sup>2-</sup> in Sn<sub>6</sub>Sb<sub>10</sub>S<sub>21</sub> [62].

In addition, depth profile analysis from the surface to the substrate of annealed sample ASTS2H reveals that the elements Sn, Sb and S are uniformly distributed throughout the depth of the thin film and are given in Fig. 8.

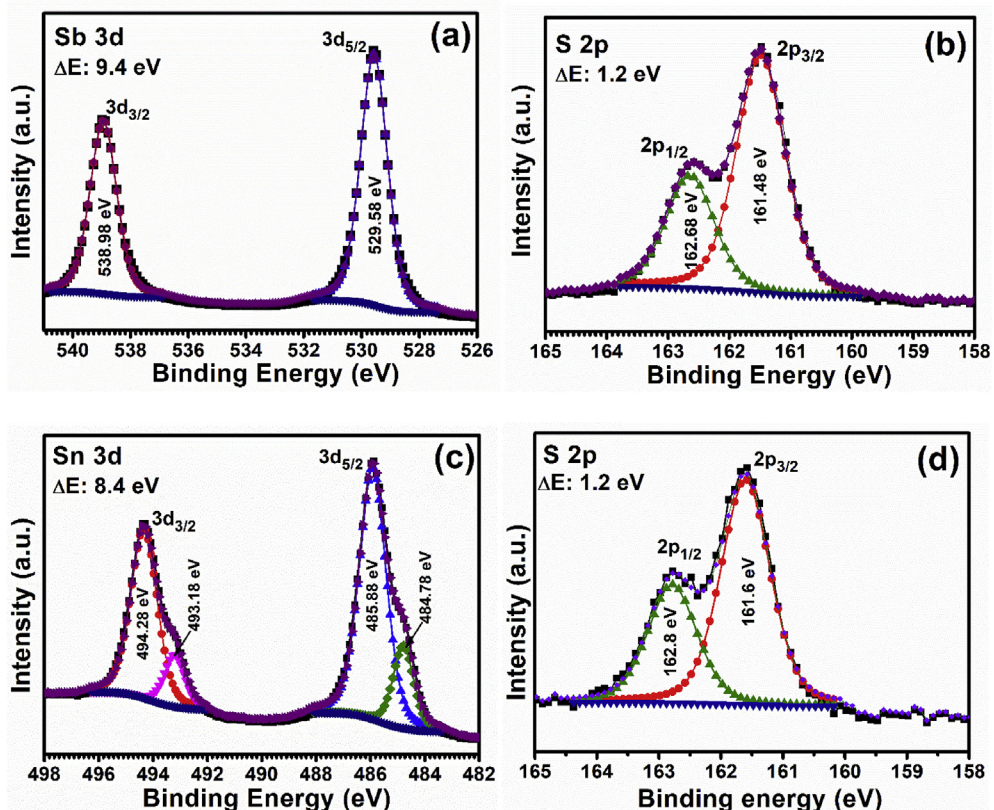


**Fig. 6.** XPS core level spectra of (a) Sb 3d and (b) S 2p in Sb<sub>2</sub>S<sub>3</sub> layer and (c) Sn 3d and (d) S 2p in SnS layer in the as-deposited ASTS thin films prepared via CBD.

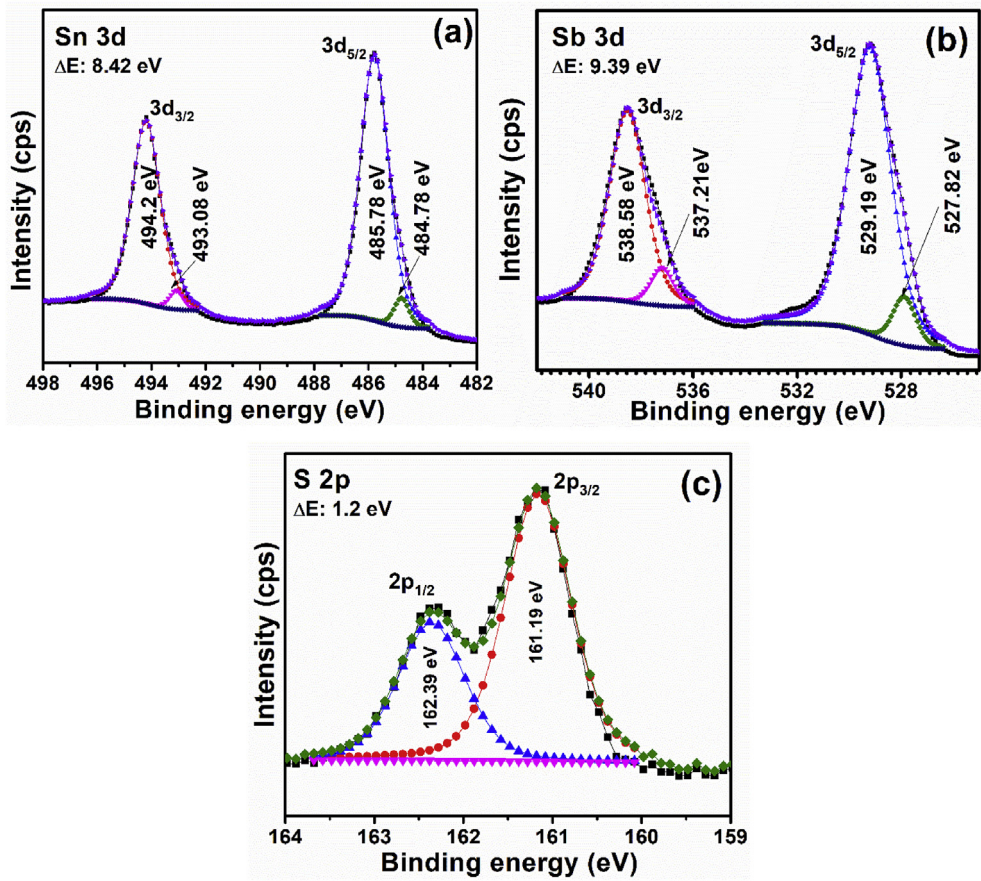


**Fig. 7.** XPS high resolution spectra of (a) Sn 3d, (b) Sb 3d and (c) S2p states in ASTS2H.

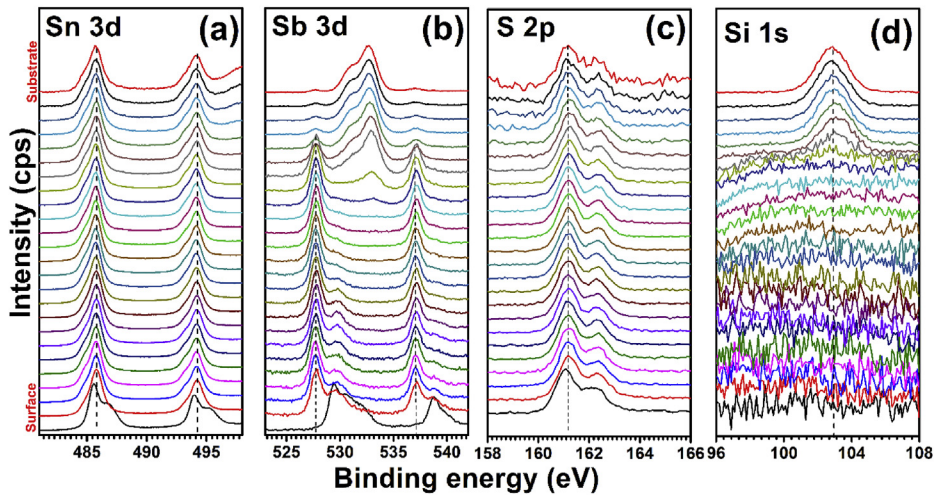


**Fig. 8.** XPS depth profile analysis in the (a) Sn 3d, (b) Sb 3d, (c) S 2p and (d) Si 1s regions for ASTS2H thin film from the surface to glass substrate.

#### 3.4. Scanning electron microscopy

We analyzed the surface morphology of the as-deposited and heat-treated ASTS thin films from scanning electron micrographs taken at a magnification of 20000 which are shown in Fig. 9(a–g). All the samples have similar morphology with interpenetrating nanosheet like structures oriented in different directions. Moreover, higher magnification images show that the cross-linked

nanosheets are compact and uniform as well as pinhole free [63]. Here, the top layer is SnS and a similar kind of morphology was detected for SnS thin films prepared by the CBD method [40,64]. At higher annealing temperatures the nanosheets appear to agglomerate at distinct places on top of the surface of the film as observed before in similar Sn–Sb–S systems [24]. The SEM images (Fig. 9) show very rough film surface. However, the rough morphology of the absorber layers can significantly influence the device

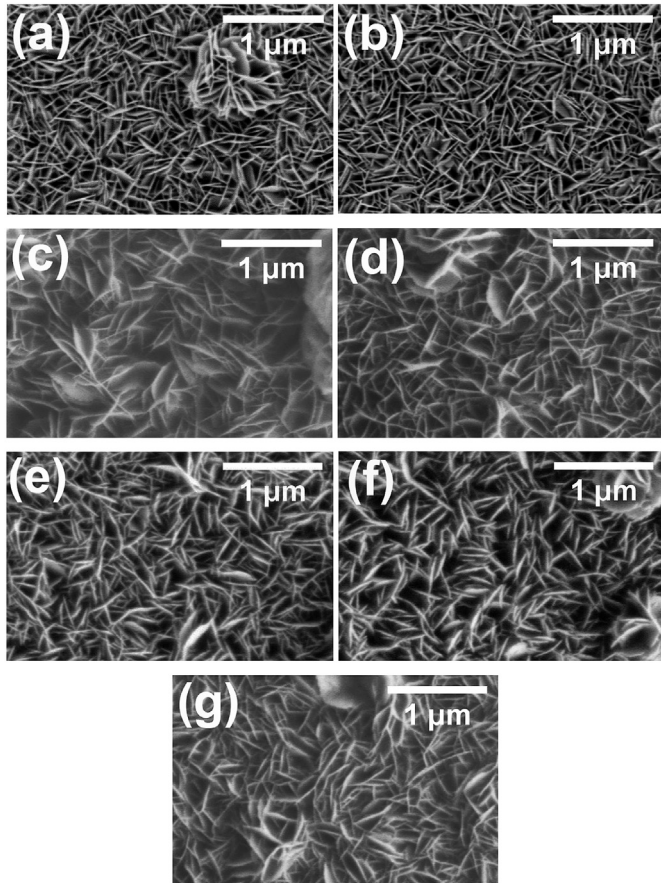


**Fig. 9.** SEM images of (a) ASTS (b) ASTS390 (c) ASTS400 (d) ASTS450 (e) ASTS1H (f) ASTS2H (g) ASTS3H thin films.

performance when trying to grow the electron/hole transport layer or an electrode on top. Such rough morphology can be modified by surface treatments using the chemical as well as physical methods. The chemical etching of rf sputtered ZnO:Al thin films using dilute hydrochloric acid resulted in more uniform textured films [65]. Rapid thermal treatment of CuSbS<sub>2</sub> thin films at 600 °C for 5 min resulted in the films with surface morphology composed of highly oriented and compact grains [66]. In this case, the nonequilibrium high-temperature processing of thin films for a very short time can result in fast grain growth without any compositional change. Nitrogen and argon plasma treatments of chemical bath deposited CdS thin films modified their surface morphology to smaller particles distributed uniformly [47]. Besides, by irradiating chemically deposited SnS thin films using a pulsed laser (532 nm) completely changed their morphology to much smoother with spherical particles [40]. Such methods can be applied to produce device quality films with uniform topological features.

### 3.5. UV–Vis–NIR spectroscopy

The UV–Vis–NIR spectroscopy was used to measure the transmittance, absorbance and reflectance spectra of the samples in the wavelength range 200–2000 nm. The spectra are illustrated in Fig. 10(a–c). The transmittance spectra in Fig. 10(a) with interference fringes falls sharply at the band edge region between 600 and 800 nm. The optical absorption coefficients were calculated from the absorption data employing the following relation [67],

$$\alpha = 2.303 \frac{A}{t} \quad (3)$$

where  $\alpha$  is the absorption coefficient, A is the absorbance and t is the thickness of the thin film.

The Tauc relation given by equation (4) was used to find the direct band gap of the thin films by plotting a graph between  $(\alpha h\nu)^2$  vs  $h\nu$  and extrapolating the linear part of the curve to the horizontal axis of photon energy at  $(\alpha h\nu)^2 = 0$  [68].

$$(\alpha h\nu)^2 = h\nu - E_g \quad (4)$$

Here,  $\alpha$  is the absorption coefficient,  $h$  is the Plank's constant,  $\nu$  is the frequency and  $E_g$  is the optical band gap. The calculated band gap values are listed in Table 3. Interestingly, the band gap values lie in the range of 1.3–1.4 eV which are excellent for photovoltaic applications.

Further, the band gaps were calculated for ASTS thin films annealed for different durations at 390 °C. As can be seen in Fig. 11(d) the band gap values calculated are 1.44, 1.26 and 1.31 eV for samples annealed for 1 h, 2 h and 3 h, respectively. The lower band gap values are a result of the improved crystallinity at 2 h annealing reducing the grain boundaries thereby better transport. Nevertheless, even longer durations deteriorate the samples resulting in the increased bandgap value. Similar bandgap values and bandgap shifts were observed for other Sn–Sb–S systems from the literature which can be seen in Table 3. The small band gap energy of Sn–Sb–S systems could be due to the narrow energy splitting between the valence band maximum (VBM) and conduction band minimum (CBM) as a consequence of different binding energies of Sb–S (379 kJ/mol) and Sn–S (464 kJ/mol) bonds. Hence, the observed results could be because of the increase in the population of heteropolar Sb–S and Sn–S bonds as well as the defective homopolar Sn–Sn bonds [22].

### 3.6. Photoconductivity

Following the better optical properties exhibited by the new Sn<sub>6</sub>Sb<sub>10</sub>S<sub>21</sub> thin films, we measured their photocurrent response with silver contacts of 5 mm length separated by 5 mm distance. The samples were kept in a black box under the illumination of a halogen lamp having 50 W for 20 s to measure the photocurrent, while the dark current was measured for 20 s before and after the illumination. During the measurements, a bias voltage of 10 V was applied, and the response obtained is depicted in Fig. 12. The curves indicate that all the samples are photoconductive.

Fig. 12(a) depicts the photocurrent response measured for the Sn<sub>6</sub>Sb<sub>10</sub>S<sub>21</sub> thin films, ASTS390, ASTS400 and ASTS450. Further, we have also observed better photoresponse for the samples after annealing at 390 °C for different durations. This photoresponse is due to the new tin antimony sulfide ternary phase which was verified from the XRD and Raman analysis. The conductivity values of the samples were in the orders of 10<sup>-4</sup> (Ωcm)<sup>-1</sup> calculated from the photoresponse. This high resistivity of the thin films is due to the increased concentration of Sb in the samples [27]. Further, the as deposited ASTS and ASTS300 samples demonstrated n-type behavior in the hot point probe method whereas the thin films treated at 350 °C and higher temperatures exhibited p-type characteristics. This bipolar conductivity arises due to the presence of native defects like vacancies and interstitials in semiconductors. It is expected that, even though more SnS diffuses into the other layer with thermal treatments, inert conditions and the low partial pressure of Sn are favorable for the creation of Sn vacancies. These vacancies in the Sn<sub>6</sub>Sb<sub>10</sub>S<sub>21</sub> structure might be responsible for this

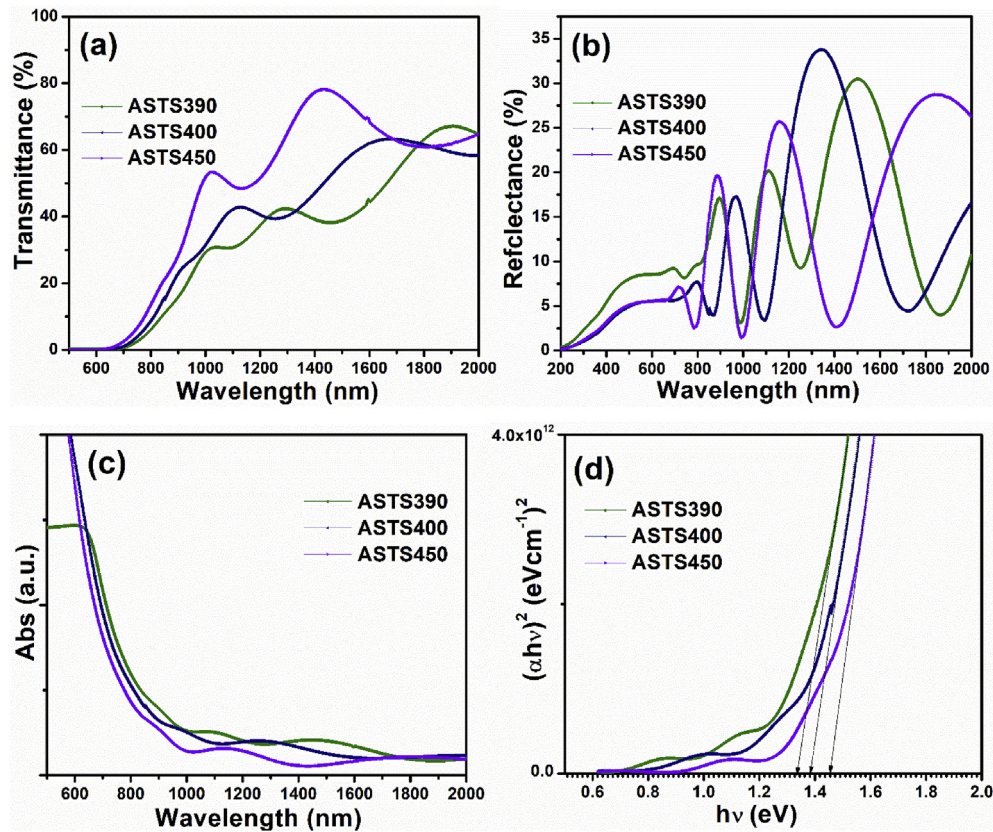


**Fig. 10.** The spectra of (a) transmittance (b) reflectance (c) absorbance measured for the ASTS thin films annealed at different temperatures (d) Tauc plot for calculation of the band gaps of thin films.

**Table 3**

The optical band gap values from the literature for various Sn–Sb–S phases.

Composition	Optical band gap (eV)	
	Direct	Indirect
SnSb <sub>2</sub> S <sub>4</sub>	1.23 [11], 2.75–1.65 [12], 1.29 [22], 2.04 [25], 1.63 [50] 1.87–1.46 [69], 2.1–1.65 [70], 1.75–2.76 [71], 1.3 [72], 1.53–1.84 [73], 1.40–1.65 [52], 2.4 [74]	1.82 [25], 1.71–1.31 [69]
SnSb <sub>4</sub> S <sub>7</sub>	1.52 [22], 2.11 [25], 1.45–1.92 [48]	1.87 [25]
Sn <sub>2</sub> Sb <sub>2</sub> S <sub>5</sub>	1.60–1.80 [13], 1.28 [22], 1.70 [25], 1.52–1.78, 1.80–1.96 [26], 1.51 [50]	1.42 [25]
Sn <sub>2</sub> Sb <sub>6</sub> S <sub>11</sub>	2.09 [25]	1.86 [25]
Sn <sub>3</sub> Sb <sub>2</sub> S <sub>6</sub>	1.67 [25], 1.47 [50], 1.47–1.18 [75], 1.44–1.66 [63]	1.42 [25]
Sn <sub>4</sub> Sb <sub>6</sub> S <sub>13</sub>	2.041–4.47 [50]	1.81 [25]
Sn <sub>6</sub> Sb <sub>10</sub> S <sub>21</sub>	(Our results)	
ASTS390	1.33	
ASTS400	1.38	
ASTS450	1.45	
ASTS1H	1.44	
ASTS2H	1.26	
ASTS3H	1.31	

conversion to p-type behavior [27]. The stoichiometry changes in tin and antimony of Sn–Sb–S based sulfosalts are believed to create native defects that can convert its semiconducting behavior from n-type to p-type and vice versa [14].

### 3.7. Photovoltaic device

After the detailed studies on Sn<sub>6</sub>Sb<sub>10</sub>S<sub>21</sub> thin films, we have fabricated photovoltaic cells by sequentially depositing CdS, Sb<sub>2</sub>S<sub>3</sub>

and SnS followed annealing. The silver paint was used for ohmic contact on top of carbon paint. The J-V characterizations were carried out on an active device area of 40 mm<sup>2</sup> and the J-V curve is shown in Fig. 13. The yielded photovoltaic parameters of the photovoltaic structure were  $V_{oc} = 409$  mV,  $I_{sc} = 1.46$  mA cm<sup>-2</sup> and FF = 0.25. Although the PV parameters are relatively low, this is the first report of a PV device with Sn<sub>6</sub>Sb<sub>10</sub>S<sub>21</sub> thin film as the absorber layer. The deteriorated device performance can be mainly attributed to very low electrical conductivity of Sn<sub>6</sub>Sb<sub>10</sub>S<sub>21</sub> thin films as

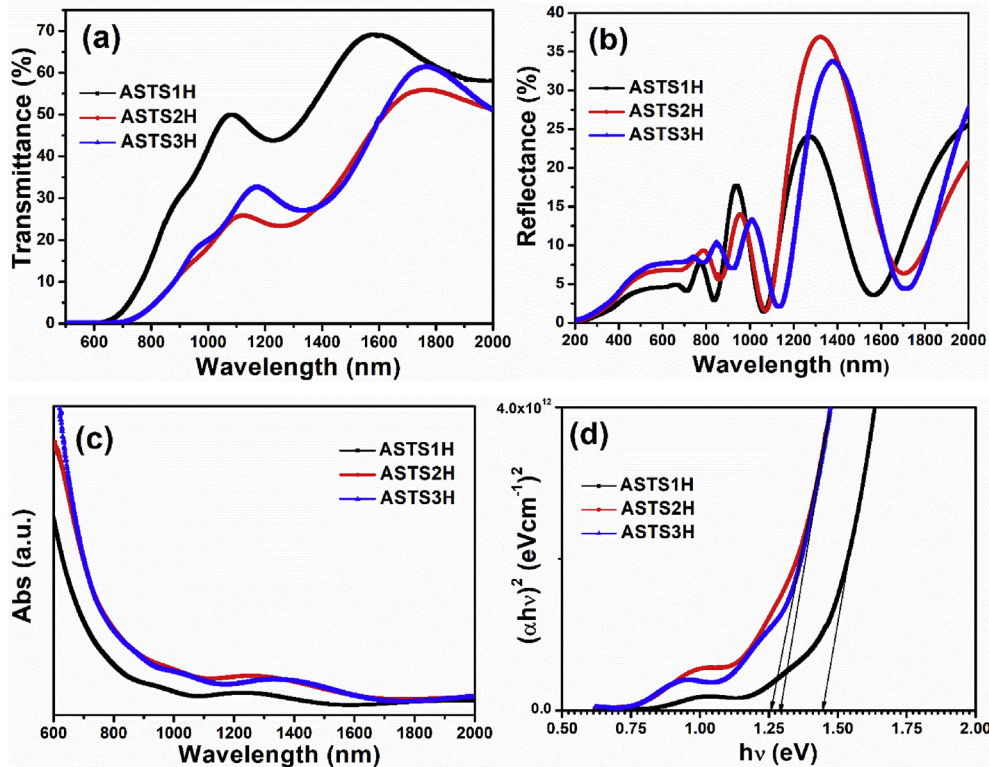


**Fig. 11.** The spectra of (a) transmittance (b) reflectance (c) absorbance for ASTS thin films annealed at 390 °C for 1 h, 2 h and 3 h. (d) Tauc plot for the calculation of band gaps of the thin films.

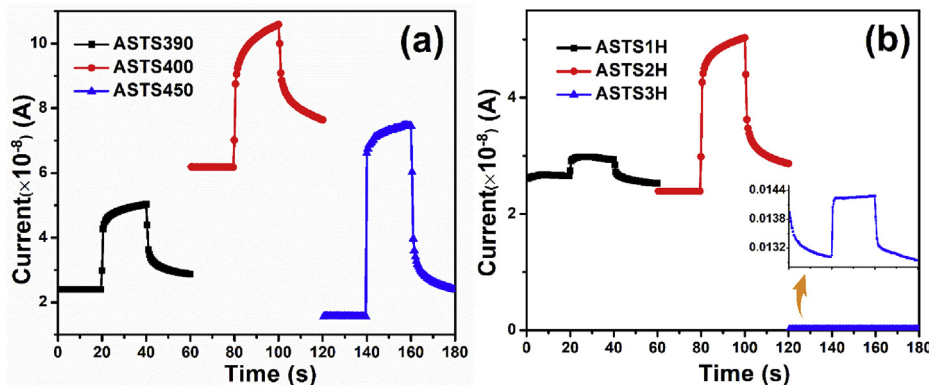


**Fig. 12.** The photoconductivity curves of ASTS thin film samples annealed at (a) 390, 400 and 450 °C for 30 min as well as (b) 390 °C for 1 h, 2 h and 3 h.

implied by the photoresponse curves. Further investigations are indeed to improve the crystallinity as well as morphology of  $\text{Sn}_6\text{Sb}_{10}\text{S}_{21}$  absorber. Post deposition treatments such as laser irradiation and rapid thermal processing are to be applied to improve the material properties [2–5]. Another reason for the poor device performance may be due to the diffusion of CdS layer into the absorber layer due to heating. To avoid the interlayer diffusion, further optimization of device structure such as substrate configuration in which CdS as buffer on the absorber followed by window layers of ZnO or ZnO:Al, can also be done. Further research is essential to improve the film properties and thus to achieve higher power conversion efficiencies for the devices as suggested.

#### 4. Conclusions

$\text{Sn}_6\text{Sb}_{10}\text{S}_{21}$  thin films were prepared via chemical bath deposition of precursor layers  $\text{Sb}_2\text{S}_3$ , SnS and subsequent thermal treatments. A systematic study involving XRD, Raman and XPS confirmed the evolution of crystal structure, phase and composition of the new absorber phase when heated ( $\geq 390$  °C) in a low vacuum. SEM images showed that the thin films morphology was composed of compact and interpenetrating vertically aligned nanosheets. The band gap values were in the range of 1.3–1.5 eV for the  $\text{Sn}_6\text{Sb}_{10}\text{S}_{21}$  phase, near optimum values for photovoltaic absorber. The device fabricated with the  $\text{Sn}_6\text{Sb}_{10}\text{S}_{21}$  absorber layer and CdS window layer on FTO coated glass showed

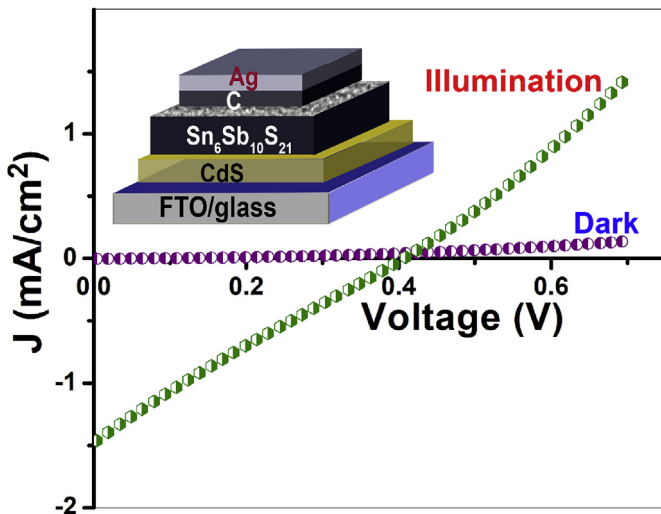


**Fig. 13.** The J-V characteristic curve of the photovoltaic device Glass/FTO/CdS/ASTS/C-Ag.

photovoltaic performance, yielding  $V_{oc} = 409$  mV,  $I_{sc} = 1.46$  mAcm $^{-2}$  and FF = 0.25. The current work essentially demands a lot of follow-up work to optimize the various parameters and combinations to explore the complete potential of Sn<sub>6</sub>Sb<sub>10</sub>S<sub>21</sub> thin films in solar cells.

#### Declaration of competing interest

There are no conflicts to declare. The manuscript was written through the contributions of all authors. All authors have given approval to the final version of the manuscript.

#### CRediT authorship contribution statement

**Sebin Devasia:** Methodology, Formal analysis, Investigation, Data curation, Visualization, Writing - original draft. **S. Shaji:** Methodology, Validation, Resources, Investigation, Writing - review & editing. **D.A. Avellaneda:** Methodology, Validation, Investigation. **J.A. Aguilar Martinez:** Methodology, Validation, Investigation. **B. Krishnan:** Conceptualization, Validation, Investigation, Resources, Supervision, Writing - review & editing, Project administration, Funding acquisition.

#### Acknowledgements

The authors acknowledge the economic support from Consejo Nacional de Ciencia y Tecnología, Mexico (CONACYT) through a project (No: C.B. 284800) for the present research. Sebin Devasia is grateful to CONACYT, Mexico for the doctoral fellowship.

#### Appendix A. Supplementary data

Supplementary data to this article can be found online at <https://doi.org/10.1016/j.jallcom.2020.154256>.

#### References

- [1] M. Kaelin, D. Rudmann, A.N. Tiwari, Low cost processing of CIGS thin film solar cells, *Sol. Energy* 77 (2004) 749–756, <https://doi.org/10.1016/j.solener.2004.08.015>.
- [2] B.M. Başol, V.K. Kapur, C.R. Leidholm, A. Halani, K. Gledhill, Flexible and light weight copper indium diselenide solar cells on polyimide substrates, *Sol. Energy Mater. Sol. Cells* 43 (1996) 93–98, [https://doi.org/10.1016/0927-0248\(95\)00171-9](https://doi.org/10.1016/0927-0248(95)00171-9).
- [3] W. Yue, F. Wei, C. He, D. Wu, N. Tang, Q. Qiao, L-Cysteine assisted-synthesis of 3D In2S3 for 3D CuInS2 and its application in hybrid solar cells, *RSC Adv.* 7 (2017) 37578–37587, <https://doi.org/10.1039/c7ra05730j>.
- [4] W. Yue, F. Wei, Y. Li, L. Zhang, Q. Zhang, Q. Qiao, H. Qiao, Hierarchical CuInS2 synthesized with the induction of histidine for polymer/CuInS2 solar cells, *Mater. Sci. Semicond. Process.* 76 (2018) 14–24, <https://doi.org/10.1016/j.mssp.2017.12.009>.
- [5] H. Kim, K. Cha, V.M. Fthenakis, P. Sinha, T. Hur, Life cycle assessment of cadmium telluride photovoltaic (CdTe PV) systems, *Sol. Energy* 103 (2014) 78–88, <https://doi.org/10.1016/j.solener.2014.02.008>.
- [6] T. Miao, D. Yu, L. Xing, D. Li, L. Jiao, W. Ma, X. Zhang, Current rectification in a structure: ReSe 2/Au contacts on both sides of ReSe 2, *Nanoscale Res. Lett.* 14 (2019) 1, <https://doi.org/10.1186/s11671-018-2843-4>.
- [7] F. Alharbi, J.D. Bass, A. Salhi, A. Alyamani, H.-C. Kim, R.D. Miller, Abundant non-toxic materials for thin film solar cells: alternative to conventional materials, *Renew. Energy* 36 (2011) 2753–2758, <https://doi.org/10.1016/j.renene.2011.03.010>.
- [8] H. Ayesha, M. Arshad, Optoelectronic Properties of Evaporated Antimony Tin Sulfide Thin Films for Solar Cell Applications, vol. 55, 2013, pp. 13129–13132.
- [9] D. Abdelkader, A. Jebali, A. Larbi, A. Harizi, M. Ben Rabeh, N. Khemiri, F. Antoni, M. Kanzari, Synthesis, characterization, structural and optical absorption behavior of Sn<sub>x</sub>Sb<sub>y</sub>S<sub>z</sub> powders, *Adv. Powder Technol.* 27 (2016) 734–741, <https://doi.org/10.1016/j.apt.2016.02.034>.
- [10] H. Dittrich, A. Städler, D. Topa, H.J. Schimper, A. Basch, Progress in sulfosalts research, *Phys. Status Solidi Appl. Mater. Sci.* 206 (2009) 1034–1041, <https://doi.org/10.1002/pssa.200881242>.
- [11] N. Ali, Z. Ali, R. Akram, S.M. Aslam, M. Jabeen, M.N. Chaudhry, M.A. Iqbal, N. Ahmad, Study of Sb<sub>28.47</sub>Tn<sub>11.22</sub>S<sub>60.32</sub> compound as thin film for photovoltaic applications, *Chalcogenide Lett.* 9 (2012) 329–335.
- [12] N. Ali, S.T. Hussain, Y. Khan, N. Ahmad, M.A. Iqbal, S.M. Abbas, Effect of air annealing on the band gap and optical properties of SnSb 2S4 thin films for solar cell application, *Mater. Lett.* 100 (2013) 148–151, <https://doi.org/10.1016/j.matlet.2013.02.097>.
- [13] M.A. Khan, A. Ahmed, N. Ali, T. Iqbal, A.A. Khan, M. Ullah, M. Shafique, Improved optical properties of tin antimony sulphide thin films for photovoltaics, *Am. J. Mater. Sci. Eng.* 4 (2016) 1–6, <https://doi.org/10.12691/ajmse-4-1-1>.
- [14] H. Dittrich, A. Bieniok, U. Brendel, M. Grodzicki, D. Topa, Sulfosalts — a new class of compound semiconductors for photovoltaic applications, *Thin Solid Films* 515 (2007) 5745–5750, <https://doi.org/10.1016/j.tsf.2006.12.071>.
- [15] Y. Moëlo, E. Makovicky, J.L. Jambor, N. Cook, A. Pring, W. Paar, E.H. Nickel, S. Graeser, S. Karup-Møller, T. Balic-Zunic, W.G. Mumme, F. Vurro, D. Topa, L. Bindl, K. Bente, M. Shimizu, Sulfosalts systematics: a review, Report of the sulfosalts sub-committee of the IMA Commission on Ore Mineralogy, *Eur. J. Mineral.* 20 (2008) 7–46, <https://doi.org/10.1127/0935-1221/2008/0020-1778>.
- [16] Q. He, S. Huang, C. Wang, Q. Qiao, N. Liang, M. Xu, W. Chen, J. Zai, X. Qian, The role of Mott-Schottky heterojunctions in Ag-Ag<sub>8</sub>S<sub>n</sub>S<sub>6</sub> as counter electrodes in dye-sensitized solar cells, *ChemSusChem* 8 (2015) 817–820, <https://doi.org/10.1002/cssc.201403343>.
- [17] J. Gutwirth, T. Wágner, E. Kotulánová, P. Bezdička, V. Perina, M. Hrdlicka, M. Vlček, Č. Drašar, M. Frumar, On RF magnetron-sputtering preparation of Ag-Sb-S thin films, *J. Phys. Chem. Solid.* 68 (2007) 835–840, <https://doi.org/10.1016/j.jpcs.2007.03.030>.
- [18] J. Wang, X. Yang, W. Hu, B. Li, J. Yan, J. Hu, Synthesis of AgBi<sub>2</sub>S<sub>3</sub> microspheres by templating method and their catalytic polymerization of alkylsilanes, *Chem. Commun.* (2007) 4931–4933, <https://doi.org/10.1039/b710832j>.
- [19] H.D.M. Hoheisel, No title, 98/28800, 1998.
- [20] P.H. Soni, M.V. Hathi, C.F. Desai, Optical band gap of Sn 0.2 Bi 1.8 Te 3 thin films, *Bull. Mater. Sci.* 26 (2003) 683–684, <https://doi.org/10.1007/BF02706763>.
- [21] O.L. Kheifets, L.Y. Kobelev, N.V. Melnikova, L.L. Nugaeva, Electrical properties of solid electrolytes with the general formula ABCD 3 (A = Ag, Cu; B = Pb, Sn; C = As, Sb; and D = S, Se), *Tech. Phys.* 52 (2007) 86–92, <https://doi.org/10.1134/S106378420701015X>.
- [22] D. Abdelkader, F. Chaffar Akkari, N. Khemiri, B. Gallas, F. Antoni, M. Kanzari, Structural and spectroscopic ellipsometry studies on vacuum-evaporated Sn<sub>2m-4</sub>Sb<sub>4</sub>S<sub>2m-2</sub> (m = 2, 3 and 4) thin films deposited on glass and Si substrates, *J. Alloys Compd.* 646 (2015) 1049–1057, <https://doi.org/10.1016/j.jallcom.2015.06.114>.
- [23] G.S.H. Dittrich, K. Herz, J. Eberhard, No title, in: Proc. 14th EU Photov. Sol. En. Conf., Barcelona, Spain, 1997, pp. 2054–2057.
- [24] J. Zhong, X. Xiao, Y. Zhang, N. Zhang, M. Chen, X. Fan, L. Chen, Rational design of Sn-Sb-S composite with yolk-shell hydrangea-like structure as advanced anode material for sodium-ion batteries, *J. Alloys Compd.* 793 (2019) 620–626, <https://doi.org/10.1016/j.jallcom.2019.04.232>.
- [25] D. Abdelkader, F. Chaffar Akkari, N. Khemiri, R. Miloua, F. Antoni, B. Gallas, M. Kanzari, Effect of SnS addition on the morphological and optical properties of (SnS)m(Sb<sub>2</sub>S<sub>3</sub>)<sub>n</sub> nano-rods elaborated by glancing angle deposition, *Phys. B Condens. Matter.* 546 (2018) 33–43, <https://doi.org/10.1016/j.physb.2018.05.016>.
- [26] A. Gassoumi, M. Kanzari, Optical, structural and electrical properties of the new absorber Sn<sub>2</sub>Sb<sub>2</sub>S<sub>3</sub> thin films, *Chalcogenide Lett.* 6 (2009) 163–170.
- [27] N. Ali, R. Ahmed, B. ul Haq, A. Shaari, R. Hussain, S. Goumri-Said, A novel approach for the synthesis of tin antimony sulphide thin films for

- photovoltaic application, *Sol. Energy* 113 (2015) 25–33, <https://doi.org/10.1016/j.solener.2014.12.021>.
- [28] N. Ali, R. Ahmed, A. Shaari, Bakhtiar-Ul-Haq, N. Ahmad, S.M. Abbas, Synthesis and characterization of Sn-Sb-S thin films for solar cell applications by sputtering techniques, *Kov. Mater. S.* 52 (2014) 219–223, <https://doi.org/10.4149/km-2014-4-219>.
- [29] N. Bennaji, R. Lahouli, Y. Fadhl, I. Mellouki, M. Kanzari, K. Khirouni, N. Yacoubi, M. Amlouk, Tuning of the electrical and thermal properties of SnSb<sub>2</sub>S<sub>4</sub>sulfosalt vacuum evaporated thin films subjected to a heat treatment for thermoelectric application, *Sensor Actuator Phys.* 281 (2018) 67–75, <https://doi.org/10.1016/j.sna.2018.08.031>.
- [30] S. Di Mare, D. Menossi, A. Salavei, E. Artigiani, F. Piccinelli, A. Kumar, G. Mariotto, A. Romeo, SnS thin film solar cells: perspectives and limitations, *Coatings* 7 (2017) 1–12, <https://doi.org/10.3390/coatings7020034>.
- [31] R. Chakraborty, V. Steinmann, N.M. Mangan, R.E. Brandt, J.R. Poindexter, R. Jaramillo, J.P. Mailoa, K. Hartman, A. Polizzetti, C. Yang, R.G. Gordon, T. Buonassisi, Non-monotonic effect of growth temperature on carrier collection in SnS solar cells, *Appl. Phys. Lett.* 106 (2015), 203901, <https://doi.org/10.1063/1.4921326>.
- [32] V. Vinayakumar, C.R.O. Hernández, S. Shaji, D.A. Avellaneda, J.A.A. Martinez, B. Krishnan, Effects of rapid thermal processing on chemically deposited antimony sulfide thin films, *Mater. Sci. Semicond. Process.* 80 (2018) 9–17, <https://doi.org/10.1016/j.mssp.2018.02.011>.
- [33] H. Deng, Y. Zeng, M. Ishaq, S. Yuan, H. Zhang, X. Yang, M. Hou, U. Farooq, J. Huang, K. Sun, R. Webster, H. Wu, Z. Chen, F. Yi, H. Song, X. Hao, J. Tang, Quasiepitaxy strategy for efficient full-inorganic Sb<sub>2</sub>S<sub>3</sub> solar cells, *Adv. Funct. Mater.* 29 (2019), 1901720, <https://doi.org/10.1002/adfm.201901720>.
- [34] W. Wang, M.T. Winkler, O. Gunawan, T. Gokmen, T.K. Todorov, Y. Zhu, D.B. Mitzi, Device characteristics of CZTSSe thin-film solar cells with 12.6% efficiency, *Adv. Energy Mater.* 4 (2014), 1301465, <https://doi.org/10.1002/aenm.201301465>.
- [35] K. Kaur, K. Arora, B. Behzad, Q. Qiao, M. Kumar, Nanoscale charge transport and local surface potential distribution to probe defect passivation in Ag doped Cu<sub>2</sub>ZnSnS<sub>4</sub> absorbing layer, *Nanotechnology* 30 (2019), 065706, <https://doi.org/10.1088/1361-6528/aa185>.
- [36] M. Azzouzi, A. Cabas-Vidani, S.G. Haass, J.A. Röhr, Y.E. Romanyuk, A.N. Tiwari, J. Nelson, Analysis of the voltage losses in CZTSSe solar cells of varying Sn content, *J. Phys. Chem. Lett.* (2019) 2829–2835, <https://doi.org/10.1021/acscjpcllett.9b00506>.
- [37] Nisika, K. Kaur, K. Arora, A.H. Chowdhury, B. Bahrami, Q. Qiao, M. Kumar, Energy level alignment and nanoscale investigation of a-TiO<sub>2</sub>/Cu-Zn-Sn-S interface for alternative electron transport layer in earth abundant Cu-Zn-Sn-S solar cells, *J. Appl. Phys.* 126 (2019), 193104, <https://doi.org/10.1063/1.5121874>.
- [38] Y. Xu, T. Gong, J.N. Munday, The generalized Shockley-Queisser limit for nanostructured solar cells, *Sci. Rep.* 5 (2015), 13536, <https://doi.org/10.1038/srep13536>.
- [39] F. Aousgi, M. Kanzari, Study of the optical properties of Sn-doped Sb<sub>2</sub>S<sub>3</sub> thin films, *Energy Procedia* 10 (2011) 313–322, <https://doi.org/10.1016/j.egypro.2011.10.197>.
- [40] D. Avellaneda, B. Krishnan, T.K. Das Roy, G.A. Castillo, S. Shaji, Modification of structure, morphology and physical properties of tin sulfide thin films by pulsed laser irradiation, *Appl. Phys. Mater. Sci. Process* 110 (2013) 667–672, <https://doi.org/10.1007/s00339-012-7148-3>.
- [41] B. Krishnan, A. Arato, E. Cardenas, T.K. Das Roy, G.A. Castillo, On the structure, morphology, and optical properties of chemical bath deposited Sb<sub>2</sub>S<sub>3</sub> thin films, *Appl. Surf. Sci.* 254 (2008) 3200–3206, <https://doi.org/10.1016/j.japsusc.2007.10.098>.
- [42] C. Garza, S. Shaji, A. Arato, E. Perez-Tijerina, G. Alan Castillo, T.K. Das Roy, B. Krishnan, p-Type CuSbS<sub>2</sub> thin films by thermal diffusion of copper into Sb<sub>2</sub>S<sub>3</sub>, *Sol. Energy Mater. Sol. Cells* 95 (2011) 2001–2005, <https://doi.org/10.1016/j.solmat.2010.06.011>.
- [43] E. Cárdenas, A. Arato, E. Perez-Tijerina, T.K. Das Roy, G. Alan Castillo, B. Krishnan, Carbon-doped Sb<sub>2</sub>S<sub>3</sub> thin films: structural, optical and electrical properties, *Sol. Energy Mater. Sol. Cells* 93 (2009) 33–36, <https://doi.org/10.1016/j.solmat.2008.02.026>.
- [44] J.G. Garza, S. Shaji, A.C. Rodriguez, T.K. Das Roy, B. Krishnan, AgSbSe 2 and AgSb(S,Se) 2 thin films for photovoltaic applications, *Appl. Surf. Sci.* 257 (2011) 10834–10838, <https://doi.org/10.1016/j.apsusc.2011.07.115>.
- [45] R.E. Ornelas-Acosta, S. Shaji, D. Avellaneda, G.A. Castillo, T.K. Das Roy, B. Krishnan, Thin films of copper antimony sulfide: a photovoltaic absorber material, *Mater. Res. Bull.* 61 (2015) 215–225, <https://doi.org/10.1016/j.materresbull.2014.10.027>.
- [46] D. Avellaneda, M.T.S. Nair, P.K. Nair, Polymorphic tin sulfide thin films of zinc blende and orthorhombic structures by chemical deposition, *J. Electrochem. Soc.* (2008), <https://doi.org/10.1149/1.2917198>.
- [47] G. Gonzalez, B. Krishnan, D. Avellaneda, G.A. Castillo, T.K. Das Roy, S. Shaji, Modification of optical and electrical properties of chemical bath deposited CdS using plasma treatments, *Thin Solid Films* (2011) 7587–7591, <https://doi.org/10.1016/j.tsf.2011.01.374>. Elsevier.
- [48] A. Jebali, N. Khemiri, M. Kanzari, The effect of annealing in N<sub>2</sub> atmosphere on the physical properties of SnSb<sub>4</sub>S thin films, *J. Alloys Compd.* 673 (2016) 38–46, <https://doi.org/10.1016/j.jallcom.2016.02.159>.
- [49] J.B. Parise, P.P.K. Smith, Structure of the tin antimony sulphide Sn<sub>6</sub>Sb<sub>10</sub>S<sub>21</sub>, *Acta Crystallogr.* C40 (1984) 1772–1776, <https://doi.org/10.1107/s0108270184009495>.
- [50] M. Ben Rabeh, N. Khedmi, M. Kanzari, Prospect for Sn<sub>n</sub>Sb<sub>2</sub>nS<sub>3</sub>n+m (n = 1, m = 1, 2, 3) sulfosalts compounds, *J. Mater. Sci. Mater. Electron.* 26 (2015) 2002–2009, <https://doi.org/10.1007/s10854-014-2531-9>.
- [51] P. Kumar, R. Thangaraj, Glassy state and structure of Sn-Sb-Se chalcogenide alloy, *J. Non-Cryst. Solids* 352 (2006) 2288–2291, <https://doi.org/10.1016/j.jnoncrysol.2006.02.041>.
- [52] M. Ben Rabeh, N. Khedmi, M. Kanzari, Vacuum annealing effects on the structural and optical properties of SnSb<sub>2</sub>S<sub>4</sub> thin films fabricated by thermal evaporation technique, *Optik* 126 (2015) 3104–3109, <https://doi.org/10.1016/j.jleo.2015.07.093>.
- [53] G.H. Tariq, K. Hutchings, D.W. Lane, K.D. Rogers, M. Anis-ur-Rehman, Annealing effects on the microstructural properties of complex sulfosalts (SnS)<sub>x</sub>-(Bi<sub>2</sub>S<sub>3</sub>)<sub>1-x</sub> gradient thin films, *J. Phys. D Appl. Phys.* 46 (2013), 485302, <https://doi.org/10.1088/0022-3727/46/48/485302>.
- [54] A. Sharmin, M.S. Bashar, M. Sultana, S.M.M. Al Mamun, Sputtered single-phase kesterite Cu<sub>2</sub>ZnSnS<sub>4</sub> (CZTS) thin film for photovoltaic applications: post annealing parameter optimization and property analysis Sputtered single-phase kesterite Cu<sub>2</sub>ZnSnS<sub>4</sub> (CZTS) thin film for photovoltaic applications: P, *AIP Adv.* 4 (2020), 015230, <https://doi.org/10.1063/1.5129202>.
- [55] E. Smith, G. Dent, Modern Raman Spectroscopy - A Practical Approach, 2005, <https://doi.org/10.1002/0470011831>.
- [56] G. Lucovsky, R.M. Martin, A molecular model for the vibrational modes in chalcogenide glasses, *J. Non-Cryst. Solids* 8–10 (1972) 185–190, [https://doi.org/10.1016/0022-3093\(72\)90134-2](https://doi.org/10.1016/0022-3093(72)90134-2).
- [57] N. Ben Mehrez, N. Khemiri, M. Kanzari, Study of structural and morphological properties of thermally evaporated Sn<sub>2</sub>B<sub>6</sub>S<sub>11</sub> thin films, *Mater. Chem. Phys.* 182 (2016) 133–138, <https://doi.org/10.1016/j.matchemphys.2016.07.014>.
- [58] E.I. Kamitsos, J.A. Kapoutsis, I.P. Culeac, M.S. Iovu, Structure and bonding in As-Sb-S chalcogenide glasses by infrared reflectance spectroscopy, *J. Phys. Chem. B* 101 (1997) 11061–11067, <https://doi.org/10.1021/jp972348v>.
- [59] L. Petit, N. Carlie, F. Adamietz, M. Couzi, V. Rodriguez, K.C. Richardson, Correlation between physical, optical and structural properties of sulfide glasses in the system Ge-Sb-S, *Mater. Chem. Phys.* 97 (2006) 64–70, <https://doi.org/10.1016/j.matchemphys.2005.07.056>.
- [60] D. Avellaneda, B. Krishnan, A.C. Rodriguez, T.K. Das Roy, S. Shaji, Heat treatments in chemically deposited Sn<sub>n</sub> thin films and their influence in Cd<sub>n</sub>/Sn<sub>n</sub> photovoltaic structures, *J. Mater. Sci. Mater. Electron.* 26 (2015) 5585–5592, <https://doi.org/10.1007/s10854-014-2295-2>.
- [61] G.G. Guillen, M.I. Mendivil Palma, B. Krishnan, D. Avellaneda Avellaneda, S. Shaji, Tin sulfide nanoparticles by pulsed laser ablation in liquid, *J. Mater. Sci. Mater. Electron.* 27 (2016) 6859–6871, <https://doi.org/10.1007/s10854-016-4639-6>.
- [62] J.F. Moulder, W.F. Stickle, P.E. Sobol, K.D. Bomben, *Handbook of X-Ray Photoelectron Spectroscopy: a Reference Book of Standard Spectra for Identification and Interpretation of XPS Data*, 1992, 9780962702624.
- [63] A. Larbi, F. Chaffar Akkari, H. Dahman, D. Demaille, B. Gallas, M. Kanzari, Structural, morphological and optical properties of Sn<sub>3</sub>Sb<sub>2</sub>S<sub>6</sub> thin films synthesized by oblique angle deposition, *J. Electron. Mater.* 45 (2016) 5487–5496, <https://doi.org/10.1007/s11664-016-4714-z>.
- [64] S. Biswas, S. Kar, S. Chaudhuri, Thioglycolic acid (TGA) assisted hydrothermal synthesis of SnS nanorods and nanosheets, *Appl. Surf. Sci.* 253 (2007) 9259–9266, <https://doi.org/10.1016/j.apsusc.2007.05.053>.
- [65] S. Fernández, O. de Abril, F.B. Narango, J.J. Gandía, High quality textured ZnO:Al surfaces obtained by a two-step wet-chemical etching method for applications in thin film silicon solar cells, *Sol. Energy Mater. Sol. Cells* 95 (2011) 2281–2286, <https://doi.org/10.1016/j.solmat.2011.03.042>.
- [66] V. Vinayakumar, S. Shaji, D. Avellaneda, T.K.K. Das Roy, G.A.A. Castillo, J.A.A.A. Martinez, B. Krishnan, CuSbS<sub>2</sub> thin films by rapid thermal processing of Sb<sub>2</sub>S<sub>3</sub>-Cu stack layers for photovoltaic application, *Sol. Energy Mater. Sol. Cells* 164 (2017) 19–27, <https://doi.org/10.1016/j.solmat.2017.02.005>.
- [67] Y. Fadhl, A. Rabhi, M. Kanzari, Effect of air annealing on dispersive optical constants and electrical properties of SnSb<sub>2</sub>S<sub>4</sub> thin films, *Mater. Sci. Semicond. Process.* 26 (2014) 282–287, <https://doi.org/10.1016/j.mss.2014.05.002>.
- [68] S. Devasia, P.V. Athma, M. Shaji, M.C.S. Kumar, E.I. Anila, Post-deposition thermal treatment of sprayed ZnO:Al thin films for enhancing the conductivity, *Phys. B Condens. Matter* 533 (2018) 83–89, <https://doi.org/10.1016/j.physb.2018.01.004>.
- [69] D. Abdelkader, M. Ben Rabeh, N. Khemiri, M. Kanzari, Investigation on optical properties of Sn<sub>x</sub>Sb<sub>y</sub>S z sulfosalts thin films, *Mater. Sci. Semicond. Process.* 21 (2014) 14–19, <https://doi.org/10.1016/j.mss.2014.01.027>.
- [70] N. Khedmi, M. Ben Rabeh, M. Kanzari, Structural morphological and optical properties of SnSb<sub>2</sub>S<sub>4</sub> thin films grown by vacuum evaporation method, *J. Mater. Sci. Technol.* 30 (2014) 1006–1011, <https://doi.org/10.1016/j.jmst.2014.03.019>.
- [71] N. Ali, S.T. Hussain, M.A. Iqbal, K. Hutchings, D. Lane, Structural and optoelectronic properties of antimony tin sulphide thin films deposited by thermal evaporation techniques, *Optik* 124 (2013) 4746–4749, <https://doi.org/10.1016/j.jleo.2013.01.086>.
- [72] A. Gassoumi, M. Kanzari, Growth and post-annealing effect on the properties of the new sulfosalts SnSb<sub>2</sub>S<sub>4</sub> thin films, *Phys. E Low-dimens. Syst. Nanostruct.* 44 (2011) 71–74, <https://doi.org/10.1016/j.phse.2011.07.007>.
- [73] Y. Fadhl, A. Rabhi, M. Kanzari, Annealing effects on the physical properties of thermally evaporated Sn<sub>2</sub>Sb<sub>2</sub>S<sub>5</sub> thin films, in: 2014 1st Int. Conf. Green

- Energy vol. 2014, ICGE, 2014, pp. 124–128, <https://doi.org/10.1109/ICGE.2014.6835409>.
- [74] A. Saeed, N. Alia, W.A. Syed, Photovoltaic effect in the metal based sulfosalts thin film deposited by physical vapor deposition technique, Chalcogenide Lett. 10 (2013) 143–150.
- [75] A. Larbi, H. Dahman, M. Kanzari, Effect of substrate temperature on structural and optical properties of the new high absorbent Sn<sub>3</sub>Sb<sub>2</sub>S thin films, Vacuum 110 (2014) 34–39, <https://doi.org/10.1016/j.vacuum.2014.08.009>.